



JES FOCUS ISSUE ON MATHEMATICAL MODELING OF ELECTROCHEMICAL SYSTEMS AT MULTIPLE SCALES IN HONOR OF JOHN NEWMAN

Direct, Efficient, and Real-Time Simulation of Physics-Based Battery Models for Stand-Alone PV-Battery Microgrids

Seong Beom Lee,^{a,*} Chintan Pathak,^{a,*} Venkatasailanathan Ramadesigan,^{b,**} Wenzhong Gao,^c and Venkat R. Subramanian^{a,d,**,z}

^aDepartment of Chemical Engineering, University of Washington, Seattle, Washington 98195, USA

^bDepartment of Energy Science and Engineering, Indian Institute of Technology Bombay, Powai, Mumbai, Maharashtra 400076, India

^cDepartment of Electrical and Computer Engineering, University of Denver, Denver, Colorado 80210, USA

^dPacific Northwest National Laboratory, Richland, Washington 99354, USA

With renewable energy based electrical systems becoming more prevalent in homes across the globe, microgrids are becoming widespread and could pave the way for future energy distribution. Accurate and economical sizing of stand-alone power system components, including batteries, has been an active area of research, but current control methods do not make them economically feasible. Typically, batteries are treated as a black box that does not account for their internal states in current microgrid simulation and control algorithms. This might lead to under-utilization and over-stacking of batteries. In contrast, detailed physics-based battery models, accounting for internal states, can save a significant amount of energy and cost, utilizing batteries with maximized life and usability. It is important to identify how efficient physics-based models of batteries can be included and addressed in current grid control strategies. In this paper, we present simple examples for microgrids and the direct simulation of the same including physics-based battery models. A representative microgrid example, which integrates stand-alone PV arrays, a Maximum Power Point Tracking (MPPT) controller, batteries, and power electronics, is illustrated. Implementation of the MPPT controller algorithm and physics-based battery model along with other microgrid components as differential algebraic equations is presented. The results of the proposed approach are compared with the conventional control strategies and improvements in performance and speed are reported.

© The Author(s) 2017. Published by ECS. This is an open access article distributed under the terms of the Creative Commons Attribution Non-Commercial No Derivatives 4.0 License (CC BY-NC-ND, <http://creativecommons.org/licenses/by-nc-nd/4.0/>), which permits non-commercial reuse, distribution, and reproduction in any medium, provided the original work is not changed in any way and is properly cited. For permission for commercial reuse, please email: oa@electrochem.org. [DOI: 10.1149/2.0031711jes] All rights reserved.



Manuscript submitted January 5, 2017; revised manuscript received February 8, 2017. Published February 23, 2017. This was Paper 413 presented at the San Diego, California, Meeting of the Society, May 29- June 2, 2016. *This paper is part of the JES Focus Issue on Mathematical Modeling of Electrochemical Systems at Multiple Scales in Honor of John Newman.*

Batteries have been integrated in microgrids to mitigate intermittent characteristics of alternative energy sources such as solar, wind, and wave, thereby enhancing grid operation and reliability.^{1,2} They are well suited for microgrid applications due to their versatility, high energy density, and efficiency.³ The cost of batteries continues to decrease while their performance and life have continued to increase.⁴ However, lithium-ion batteries, which are the most widely used energy storage systems implemented in microgrids today, are still the most expensive component, accounting for about 60% of the overall Capital Expenditure (CapEx).⁵ Conservative operations in current microgrids cause high cost and low energy efficiency, underutilizing and overstacking batteries. The current microgrid controls cannot utilize batteries aggressively to achieve high penetration of renewables and maximize life and usability of batteries in the meantime. They implement empirical/equivalent-circuit battery models, treating batteries as just a black box, which does not account for its internal states, and place batteries in a small portion of the entire microgrid, which means current microgrids do not consider batteries principal components.⁶⁻¹⁰ For example, if the internal temperature of the battery is not modeled, then the battery must be operated at very low rates to ensure that the internal temperature does not reach high enough values that reduce battery life and create unsafe operating conditions. Control systems based on measured external temperatures and empirical/equivalent-circuit models must be operating conservatively to avoid potential hot spots in the internal temperature.⁶ It is evident that a tremendous amount of energy will be lost when batteries are conservatively operated. In contrast, detailed physics-based battery models, accounting for internal states, can help save an enormous amount of energy, utilizing batteries with maximized life and usability. In typical microgrid

controls, however, the computation time will significantly increase when more detailed physics-based battery models are coupled to the entire microgrid system.

There is significant literature in simulation and control of grid and renewable grid components. This has been typically a field of electrical engineering. For example, the method used to integrate the models across different devices in the microgrid typically depends on (1) the choice/convenience of users and (2) linear models and linear control schemes, which have been used for robustness, ease of use for the researchers, and scalability to a large number of devices and systems. Unfortunately, battery models are highly nonlinear in nature, and linearization compromises the accuracy, leading to a narrower range of use for applications.¹¹ In this paper, we show that perhaps a better way to integrate battery models is to write the microgrid equations in mathematical form and then identify an efficient way to solve those models simultaneously with battery models. In this paper, we first show that direct Differential Algebraic Equation (DAE) implementation and simulation of microgrids gives better results regarding accuracy, simplicity, and speed, as illustrated for a simple microgrid. Next, we present how efficient the direct DAE implementation of a stand-alone PV microgrid system is, under dynamic irradiance (PV: Photovoltaic). Finally, we have identified the gain in CPU time and the energy use by directly solving physics-based battery models with the DAE implementation in microgrid models.

Modeling and Simulation of PV Arrays & MPPT Controller

In this section, we compare one of the traditional Perturb and Observe (P&O) algorithms to a DAE-based algorithm for Maximum Power Point Tracking (MPPT) in a hypothetical microgrid architecture, consisting of PV arrays and MPPT controllers, as shown in Figure 1. We show that our depiction of MPPT algorithm as DAEs can be easily and efficiently simulated using DAE solvers. We report

*Electrochemical Society Student Member.

**Electrochemical Society Member.

^zE-mail: vsubram@uw.edu

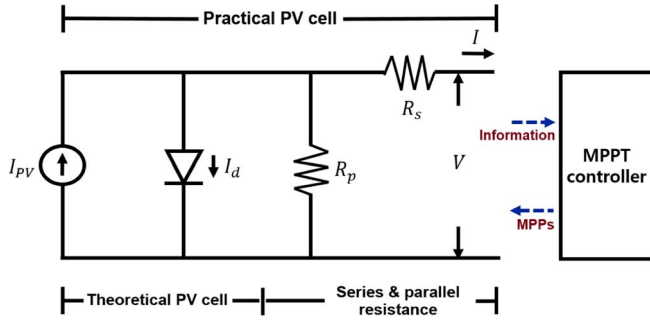


Figure 1. Single-diode equivalent circuit-based model of a practical PV cell and MPPT controller.

that the DAE-based MPPT algorithm, which enables high accuracy, simplicity, and low computation time, would facilitate maximized PV power output and simultaneous simulation of microgrid system. All simulations in this paper were carried out on a workstation with dual 8-core 3.1 GHz Intel Xeon processors with 32 GB RAM using Maple software.

Mathematical modeling for PV arrays.—PV arrays generate power by converting solar energy directly to electricity. Typically, simulation of equivalent circuit-based models featuring one to three diodes has been the common approach to predict the PV arrays' performance.¹² For mathematical modeling of PV arrays, a single-diode equivalent circuit-based model is used (see Figure 1). This model offers a good balance between simplicity and accuracy by adjusting parameters and modifying the saturation current function to match the open-circuit voltage of the model with experimental data from the solar arrays for a broad range of temperatures. The I-V characteristics of the practical PV device, consisting of multiple cells in a parallel-series combination, is given as:¹³

$$I = I_{PV} - I_0 \left[\exp \left(\frac{V + R_s I}{V_t a} \right) - 1 \right] - \frac{V + R_s I}{R_p} \quad [1]$$

I is the PV arrays' output current, I_{PV} is the PV current, I_0 is the saturation current, and V_t is the thermal voltage. These variables are temperature-dependent, but simulation and control are conducted under the assumption that temperature is a constant (see Table III). V is the PV arrays' output voltage, R_s is the series resistance, R_p is the parallel resistance, and a is the diode ideality constant. Meanwhile, the PV arrays' output current and voltage and PV current in Equation 1 can be expressed as a function of time by substituting $I = I(t)$, $I_{PV} = I_{PV}(t)$, and $V = V(t)$ as follows:

$$I(t) = I_{PV}(t) - I_0 \left[\exp \left(\frac{V(t) + R_s I(t)}{V_t a} \right) - 1 \right] - \frac{V(t) + R_s I(t)}{R_p} \quad [2]$$

All additional equations, variables, and parameters are shown in Table I, II, and III, respectively.¹³

Table I. Equations for PV systems.

Governing equation	Additional equation
$I(t) = I_{PV}(t) - I_0 \left[\exp \left(\frac{V(t) + R_s I(t)}{V_t a} \right) - 1 \right] - \frac{V(t) + R_s I(t)}{R_p}$	$V_t = \frac{N_s \cdot k \cdot T}{q}$
$\frac{I(t)}{V(t)} = \frac{I_0 \cdot \left(1 - \frac{R_s \cdot I(t)}{V(t)} \right) \cdot \exp \left(\frac{V(t) + R_s I(t)}{V_t a} \right)}{V_t a} + \frac{1 - \frac{R_s \cdot I(t)}{V(t)}}{R_p}$	$I_{PV}(t) = I_{PV,n} + \frac{K_I(T - T_n) \cdot G(t)}{G_n}$
	$I_0 = \frac{I_{sc,n} + K_I(T - T_n)}{\exp \left(\frac{V_{oc,n} + K_V(T - T_n)}{a V_t} \right) - 1}$

Table II. Variables for PV systems.

Symbol	Variables	Units
$I(t)$	PV arrays output current	A
$I_{PV}(t)$	PV currents	A
$V(t)$	PV arrays output voltage	V
$G(t)$	Insolation	W/m ²
$P(t)$	Power Output	W

Table III. Parameters for PV systems.

Symbol	Parameter	Values	Units
R_s	Series resistance	0.221	Ω
a	Diode constant	1.3	—
R_p	Parallel resistance	415.405	Ω
N_s	Series-connected cells	54	—
k	Boltzmann constant	$1.3806503 \times 10^{-23}$	J/K
q	Electron charge	$1.60217646 \times 10^{-19}$	C
K_I	Current coefficient	0.0032	A/K
T_n	Nominal temperature	298.15	K
G_n	Nominal irradiation	1000	W/m ²
$I_{sc,n}$	Nominal short-circuit current	8.21	A
$V_{oc,n}$	Nominal open-circuit voltage	32.9	V
K_V	Voltage coefficient	-0.123	V/K
$I_{PV,n}$	Light-generated current at the nominal condition	8.214	A
T	Temperature	298.15	K

P&O MPPT algorithm.—MPPT controllers can find Maximum Power Points (MPPs), and help PV arrays to produce peak power outputs. Various conventional MPPT algorithms such as P&O and Incremental Conductance (ICond) have widely been implemented as feedback algorithms. The P&O has been one of the most commonly used MPPT algorithms to track MPPs.¹⁴ The P&O algorithm applies iterative processes toward MPPs by adjusting the output voltage of PV arrays with time and voltage step. The PV power at the present instant is obtained by measuring the value of the PV voltage and current, and the power at a future instant is compared to the present power after increasing or decreasing the voltage step. In the case of positive ΔP (difference in values between the future power and present power), the algorithm operates PV systems toward the optimal point by adding the voltage step. Otherwise, if ΔP is negative, the voltage value of the optimal point is determined by subtracting the voltage step. In the P&O algorithm, as the time step increases, simulation time decreases, while accuracy decreases, and vice versa.¹⁵ Also, the range of oscillation has a proportional relationship with the voltage step.¹⁵ The flow chart of the P&O algorithm is presented in Figure 2.

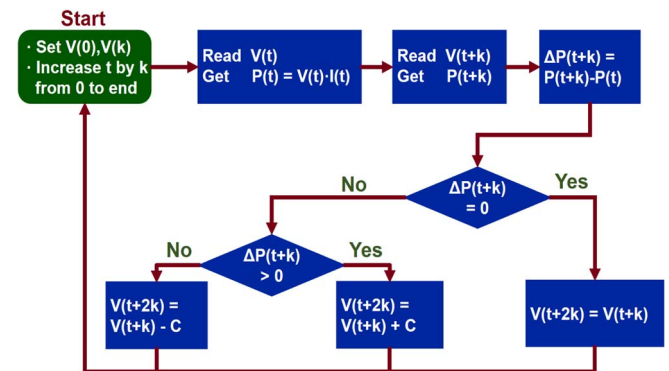


Figure 2. The flow chart of P&O MPPT algorithm. A trade-off occurs between the time/voltage step and accuracy. Therefore, it is important to determine the appropriate time/voltage step to achieve the best performance under the given environmental condition.

Even though the P&O algorithm is not able to track true MPPs, loses some amount of power due to oscillation around the MPP, and fails to track true MPPs because of its slow response to rapidly changing environmental conditions, the algorithm is the most popular, thanks to its simplicity and low hardware cost.¹⁶⁻²⁰

DAE-based MPPT algorithm.—In this section we present a DAE-based implementation of MPPT algorithm. MPPs can be calculated from the following formula²¹

$$\frac{dP(V)}{dV} = \frac{d(I(V) \cdot V)}{dV} = 0 \tag{3}$$

in which $P(V)$ is the PV arrays' output power, $I(V)$ is the PV arrays' output current, and V is the PV arrays' output voltage. Note that both $P(V)$ and $I(V)$ are functions of the output voltage. We get Equation 4 by arranging Equation 3 as follows:

$$\frac{dI(V)}{dV} = -\frac{I(V)}{V} \tag{4}$$

Also, the PV arrays' output current in Equation 1 can be expressed as a function of voltage by substituting $I = I(V)$ as follows:

$$I(V) = I_{pV} - I_0 \left[\exp\left(\frac{V + R_s I(V)}{V_t a}\right) - 1 \right] - \frac{V + R_s I(V)}{R_p} \tag{5}$$

By differentiating Equation 5 with respect to V , we get

$$\frac{dI(V)}{dV} = -\frac{I_0 \cdot \left(1 + R_s \cdot \frac{dI(V)}{dV}\right) \cdot \exp\left(\frac{V + R_s I(V)}{V_t a}\right)}{V_t a} - \frac{1 + R_s \cdot \frac{dI(V)}{dV}}{R_p} \tag{6}$$

By substituting Equation 4 into Equation 6, we get

$$\frac{I(V)}{V} = \frac{I_0 \cdot \left(1 - \frac{R_s \cdot I(V)}{V}\right) \cdot \exp\left(\frac{V + R_s I(V)}{V_t a}\right)}{V_t a} + \frac{1 - \frac{R_s \cdot I(V)}{V}}{R_p} \tag{7}$$

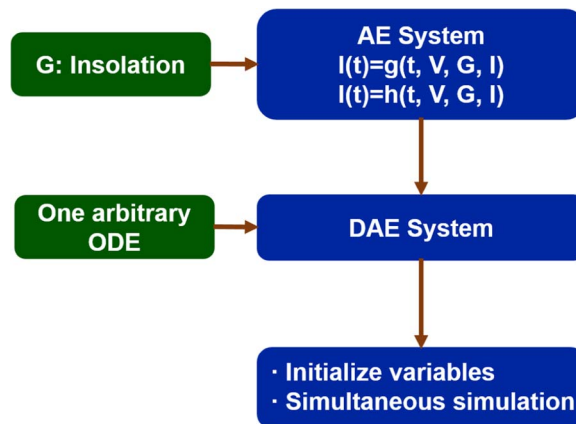


Figure 3. The flow chart of DAE-based MPPT algorithm. Proposed approach is 12 times faster than the P&O algorithm with higher accuracy (~1% more power) under the dynamic irradiance condition.

Finally, substituting $I(V) = I(t)$, $V = V(t)$ in Equation 7 gives

$$\frac{I(t)}{V(t)} = \frac{I_0 \cdot \left(1 - \frac{R_s \cdot I(t)}{V(t)}\right) \cdot \exp\left(\frac{V(t) + R_s I(t)}{V_t a}\right)}{V_t a} + \frac{1 - \frac{R_s \cdot I(t)}{V(t)}}{R_p} \tag{8}$$

The DAE-based MPPT algorithm consists of two Algebraic Equations (AEs) in two variables (Equations 2 and 8; voltage and current as a function of time, respectively). The system's response time will significantly slow down in a real situation that involves dynamic environmental condition and long time-scale. For instance, one can use nonlinear equations solvers in computational software programs such as Maple, Maplesim, Matlab, and Simulink. However, it would fail or need significantly high computation time due to the solvers' approach in finding the solution.²² Here, we implement the DAE-based MPPT algorithm consisting of AEs only. In this case, one arbitrary Ordinary Differential Equation (ODE) (Equation 9), which does not affect any processes of the entire microgrid system, can be added to convert the

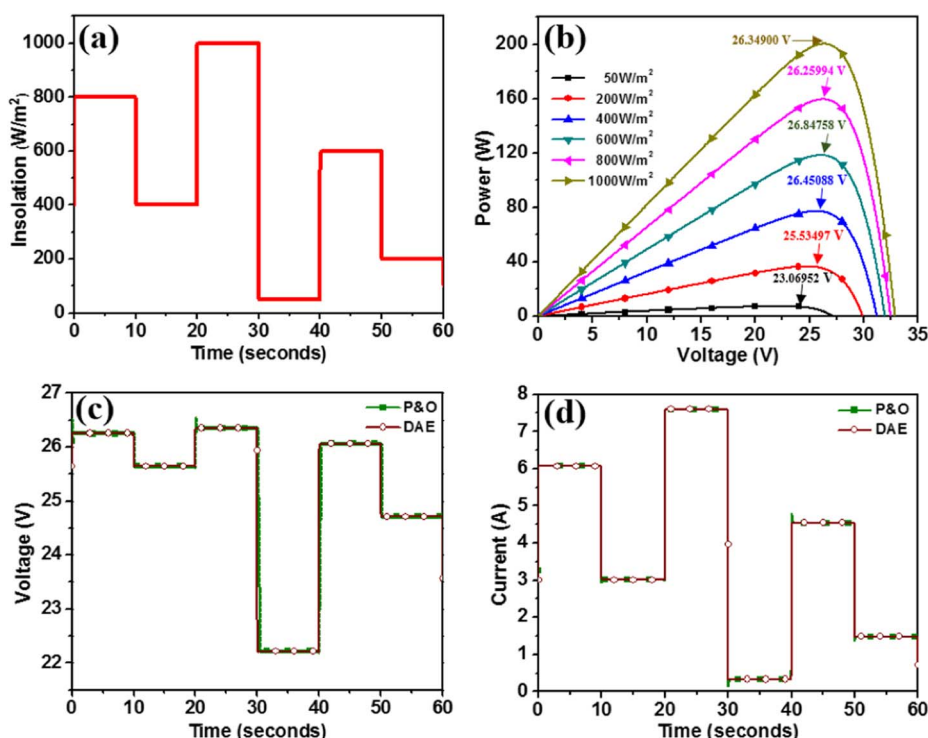


Figure 4. Simple case study with different irradiance values. (a) Solar irradiance at 800, 400, 1000, 50, 600, and 200 W/m² for 10 seconds, respectively. (b) Solar power outputs over voltage from the single-diode equivalent circuit-based model. (c) Voltage outputs (d) Current outputs, from DAE-based (wine color and empty circle) and P&O (dark green color and filled square) MPPT algorithms. In this simulation, the P&O algorithm produces the same power as the proposed DAE-based algorithm, but computation cost is ~224 times higher.

AE system into a DAE system as shown in Figure 3.

$$\frac{dy(t)}{dt} = 1 \quad [9]$$

Results.—An example of a short time simulation with the P&O and DAE-based MPPT algorithm is shown in Figure 4. This will help analyze the DAE-based algorithm's performance including its accuracy, reliability, and computation time. The voltage and time step in the P&O algorithm were adjusted (0.01 V and 0.001 s) to produce high accuracy, thereby explicitly identifying the CPU time difference between the P&O and DAE-based MPPT algorithms. Equations 2, 8, and 9 were implemented for the DAE-based MPPT algorithm. At the beginning of the simulation, when $t = 0$, the irradiance is assumed to be 400 W/m^2 and it is increased up to 800 W/m^2 within a very short time. After that, the irradiance is kept at 800, 400, 1000, 50, 600, and 200 W/m^2 for 10 seconds each and decreased to 100 W/m^2 as illustrated in Figure 4a. Even though the whole time scale is small (60 seconds), rapidly changing irradiance from 50 to 1000 W/m^2 was tested for the P&O and DAE-based MPPT algorithms' reliability. Also, solar output powers are plotted over voltage outputs at each irradiance level from Equation 5 as shown in Figure 4b. In Figures 4c and 4d, voltage and current output responses are presented by implementing the P&O and DAE-based MPPT algorithms. All MPPs in Figure 4b were rounded off to the 6th decimal place, and all the values of MPPs from the DAE-based MPPT algorithm at each irradiance level exactly matched to the results from Equation 5 with low CPU time ($\sim 0.125 \text{ s}$). On the other hand, the CPU time of the P&O algorithm was significantly slower (27.971 s) than the DAE-based MPPT algorithm with lesser accuracy. This case study clearly illustrates the DAE-based MPPT algorithm's high accuracy, reliability, and computational speed over the traditional P&O MPPT algorithm.

Modeling of PV Arrays with MPPT Controller & Power Electronics Components

In this section, we present a system with a bidirectional DC/DC converter and bidirectional DC/AC inverter (DC: Direct Current, AC: Alternative Current) that are added to the PV arrays, as shown in Figure 5. We compare combined PV systems' performance between the P&O

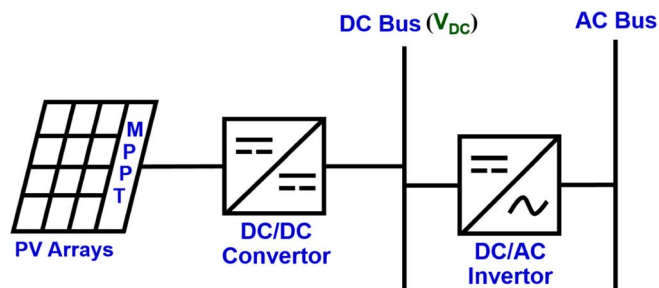


Figure 5. System configuration of a stand-alone PV microgrid, consisting of PV systems, a bidirectional DC/DC converter, a bidirectional DC/AC inverter.

and DAE-based MPPT algorithms with mathematical models of power electronics in PV microgrids under the dynamic irradiance condition. Raw irradiance data were chosen from NREL's Measurement and Instrumentation Data Center (MIDC) based on ten-minute resolution data²³

Power electronics components.—A bidirectional DC/DC converter is used for PV systems, stepping up/down voltages from its input to output. It regulates output voltages and maintains a constant voltage across DC bus from varying voltages of PV systems under the assumption that there are no energy losses. Here, the voltage value (V_{dc}) across the DC bus was fixed at 100 V, which was accomplished by increasing or decreasing the duty cycle, which is performed by using Pulse Width Modulation (PWM) of the square-wave pulses to the switches of the DC/DC converter.²⁴ The equations implemented for the bidirectional DC/DC converter are:²⁵

$$I_{dc, PV}(t) = (1 - D_{PV}(t)) \cdot I_{PV, out}(t) \quad [10]$$

$$V_{dc} = \frac{1}{1 - D_{PV}(t)} V_{PV, out}(t) \quad [11]$$

$I_{dc, PV}(t)$ is the DC bus current, $V_{PV, out}(t)$ is the output voltage, $I_{PV, out}(t)$ is the output current, and $D_{PV}(t)$ is the duty ratio of the DC/DC converter, from PV systems. A bidirectional DC/AC inverter,

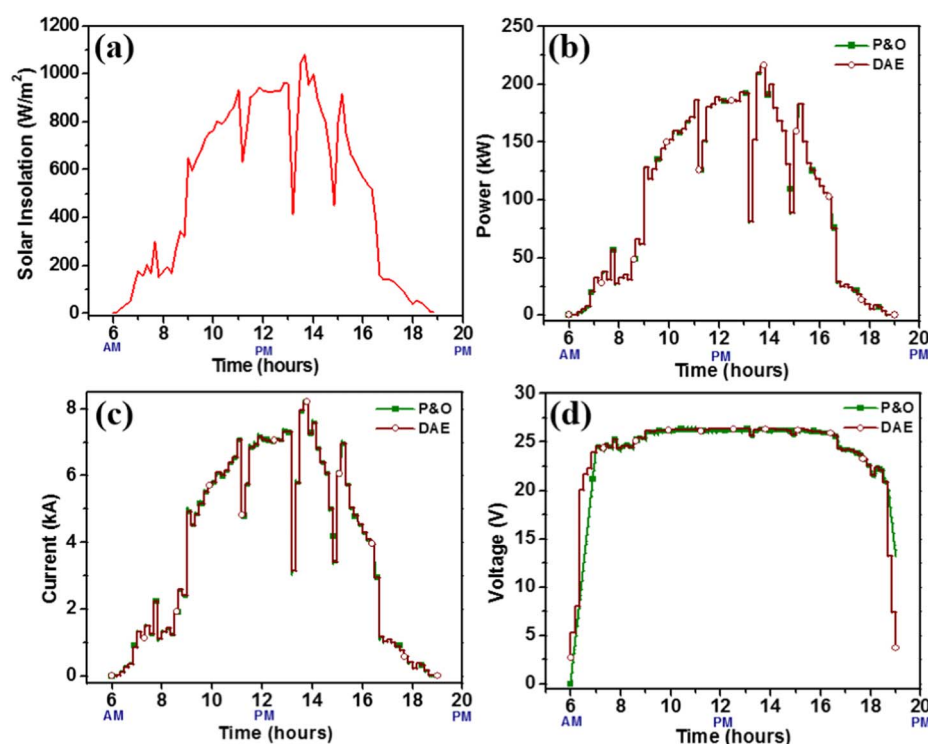


Figure 6. Comparison of voltage, current and power outputs between P&O and DAE-based MPPT algorithm. (voltage step = 0.1 V, time step = 15 seconds) (a) Solar irradiance in LA in April 10th, 2010. (b) Power outputs (c) Current outputs (d) Voltage outputs, from the proposed DAE (wine color and empty circle) and P&O (dark green color and filled square) MPPT algorithms. In (b), the proposed approach produces $\sim 1\%$ more power than the P&O algorithm for a single day. These small differences accumulate over time resulting in significant energy and cost savings. In (c) and (d), the DAE-based algorithm can track MPPs much quickly and has no oscillations compared to the P&O algorithm.

Table IV. Calibration of P&O algorithm by adjusting voltage and time step.

Voltage step (V)	CPU time (s) & Power (kW)	Time step (s)				
		1	5	10	15	20
0.05	CPU time	168.965	26.863	12.855	8.502	6.006
	Power	1308.834	1308.540	1305.880	1297.877	1287.782
0.1	CPU time	171.133	27.955	13.011	8.767	6.208
	Power	1308.792	1308.682	1308.441	1307.965	1305.725
0.5	CPU time	171.632	27.753	14.196	9.094	6.272
	Power	1306.564	1306.424	1306.249	1306.073	1305.810
0.1	CPU time	173.566	27.285	13.276	8.487	6.302
	Power	1301.177	1300.970	1300.711	1300.452	1300.124

which changes DC to AC or AC to DC, is implemented, since most standard appliances run on AC on the consumer side. Here, the conversion efficiency (η) is fixed as 0.85.

$$P_{out, PV}(t) = \eta \cdot P_{in, PV}(t) \quad [12]$$

$P_{out, PV}(t)$ is the output power from the DC/AC inverter, and $P_{in, PV}(t)$ ($= V_{dc} \cdot I_{dc, PV}(t)$) is the input power from the DC/DC converter connected to PV systems.

Results.—The MPPT simulation for PV arrays was conducted for a single day in LA, in April 2010 as shown in Figure 6. PV arrays were scaled up to kilowatt-scale systems. Figure 6a shows that the sun rises at 6 AM, and solar irradiance rises and falls until 7 PM. Under the rapidly changing environmental conditions, voltage and time step in the P&O algorithm need to be calibrated to produce the best performance as shown in Table IV. When the voltage step is 0.1 V, the maximum power output is generated, and computation time decreases with a small decrease in power as the time step increases. In other words, when the time step is increasing from 5 to 20 seconds, power outputs are the maximum in the voltage step of 0.1 V. Also, the time step of 15 seconds has a good balance between computation time and power outputs. Accordingly, the time and voltage step are fixed as 15 seconds and 0.1 V, respectively. For the DAE-based MPPT algorithm, Equations 2, 8, 9, 10, 11, and 12 were implemented. The DAE-based MPPT simulation's total CPU time is 0.702 seconds, which is 12 times faster than the P&O algorithm with more power (P&O: 1307.96 kWh, DAE: 1308.89 kWh), as shown in Figure 6b. Also, while the P&O produces oscillations around MPPs (see Figures 6c and 6d), the DAE-based MPPT algorithm precisely follows MPPs. It is evident that the amount of energy loss will increase as the PV systems' scale increases.

Modeling of PV Arrays with MPPT Controller, Battery & Power Electronics Components

Batteries and power electronics components connected to the batteries are added to the system explained in Modeling of PV arrays with MPPT controller & power electronics components section, as shown in Figure 7,²⁴ representing a typical microgrid with generation and storage. In this section, we show the performance of the reformulated Pseudo-2-Dimensional (P2D) battery model²⁶ with the DAE-based MPPT algorithm in this PV-Battery microgrid. All simulations were conducted under the same environmental conditions as in the previous section. A single-step solution approach has been applied in this large simulation, which allows for DAEs in microgrid controls to be solved without a priori knowledge of exact initial conditions for algebraic variables.²⁷

Conventional and proposed control algorithms.—Implementation of highly non-linearized DAEs in detailed battery models with MPPT feedback algorithms such as P&O and ICond causes a significant time-delay as the controls consume computation time at every time step.^{28–30} However, once the DAE-based MPPT algorithm is efficiently simulated as illustrated in the earlier sections, adding efficient

models for batteries is straightforward. The mathematical structure of the DAE-based MPPT helps easily add battery and power electronic models in the microgrid architecture (see Equations 2 and 8). For example, even the reformulated P2D model, one of the highly non-linearized DAE battery systems, which includes several important internal variables simulated at a reasonable computation time,²⁶ can be simply incorporated into the DAE-based MPPT algorithm, power electronics, and PV arrays mathematical models. Instead of adding one arbitrary equation (Equation 9), the combination of reformulated P2D battery, power electronics, PV arrays, and the DAE-based MPPT mathematical models, which includes several ODEs and AEs, becomes a system of DAEs as shown in Figure 8. The DAE solvers in the computational software allow the entire microgrid system to be simulated simultaneously with high accuracy and low computation time under rapidly changing environmental conditions.^{22,31} As more detailed physics-based battery models are involved in the entire microgrid, the DAE-based MPPT algorithm will be better suited for simultaneous simulations under real environmental conditions.

Reformulated P2D battery model.—An ideal battery model would provide good prediction while maintaining minimal computational cost. The porous electrode P2D model, which is one of electrochemical engineering models, includes several significant internal variables and has a predictive capability for battery simulations.^{32,33} The P2D model is one of the most accurate and experimentally validated physics-based battery models that allows for modeling of critical internal states used in the literature. The simulations are conducted on a mathematically reformulated P2D model that enables entire microgrid simulations to be solved in a reasonable time.^{26,33} High accuracy and short computation time of the reformulated P2D model are well suited for grid applications.³⁴ The reformulated model discretizes dependent variables as a series of trial functions, rather than a finite difference approach, using coordinate transformation and orthogonal collocation.²⁶ Also, the Solid Electrolyte Interphase (SEI) layer

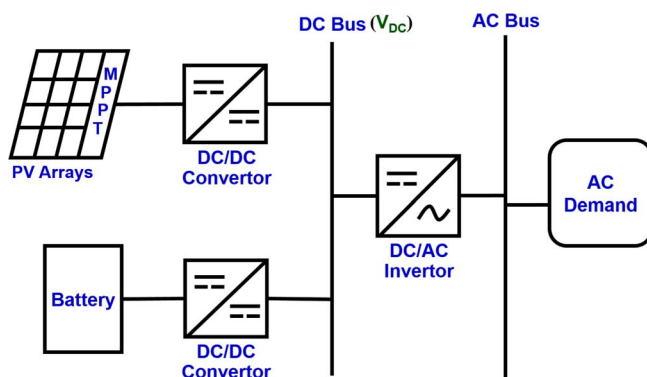


Figure 7. System configuration of a stand-alone PV-Battery microgrid, consisting of PV systems, bidirectional DC/DC converters, a bidirectional DC/AC inverter, and batteries.

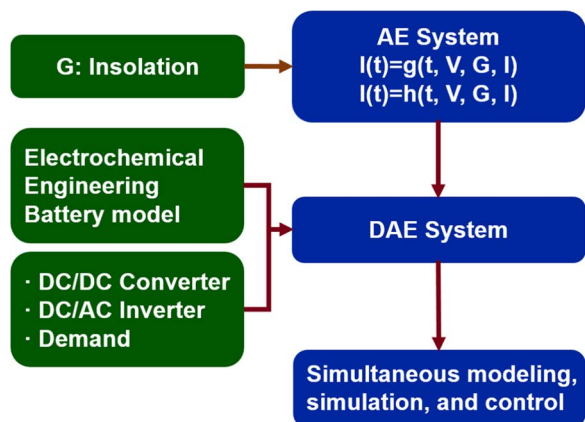


Figure 8. Simultaneous modeling, simulation, and control of microgrids, including DAE-based MPPT algorithm and electrochemical engineering battery model. Implementation of physics-based battery models incorporating current microgrid controls consumes considerable computation time. This is perhaps one of the reasons why empirical battery models are commonly used in grid communities. The proposed direct DAE implementation approach enables real-time simulation of physics-based models in microgrids.

is modeled by considering irreversible side reactions. During charging operations, some of the cyclable lithium ions are removed by reactions between the lithium ions and electrolyte, and the reactions create a passivation layer around the anode, which is described by Butler-Volmer kinetics (see Table VI).^{35,36} Equations, variables, and parameters related to the reformulated P2D model are arranged in Tables V–VIII.^{26,32,33,35,36}

Simulation of battery operation.—Batteries are charged through the power from the PV arrays converted by the DC/AC inverter and discharged based on users' demands on the microgrid. The solar en-

Table VI. Additional equations for Li-ion P2D model.

$$U_p = \frac{-4.656 + 88.669\theta_p^2 - 401.119\theta_p^4 + 342.909\theta_p^6 - 462.471\theta_p^8 + 433.434\theta_p^{10}}{-1 + 18.933\theta_p^2 - 79.532\theta_p^4 + 37.311\theta_p^6 - 73.083\theta_p^8 + 95.960\theta_p^{10}}$$

$$j_p = 2c^{0.5} \cdot k_p \cdot c^s|_{r=R_p} \left(c_{\max,p}^s - c^s|_{r=R_p} \right)^{0.5} \sinh\left(\frac{\alpha F}{RT}(\Phi_1 - \Phi_2 - U_p)\right)$$

$$j_n = 2c^{0.5} \cdot k_n \cdot c^s|_{r=R_n} \left(c_{\max,n}^s - c^s|_{r=R_n} \right)^{0.5} \sinh\left(\frac{\alpha F}{RT}\left(\Phi_1 - \Phi_2 - U_n - \frac{\delta \cdot F \cdot (j_n + j_{SEI})}{\kappa_{SEI}}\right)\right)$$

$$U_n = 0.7222 + 0.1387\theta_n + 0.029\theta_n^{0.5} - \frac{0.0172}{\theta_n} + \frac{0.0019}{\theta_n^{1.5}} + 0.2808 \exp(0.90 - 15\theta_n) - 0.7984 \exp(0.4465\theta_n - 0.4108)$$

$$\kappa_{eff,i} = \varepsilon_i^{brugg} \left(4.1253 \times 10^{-2} + 5.007 \times 10^{-4} c - 4.7212 \times 10^{-7} c^2 + 1.5094 \times 10^{-10} c^3 - 1.6018 \times 10^{-14} c^4 \right),$$

$$i = p, s, n$$

$$D_{eff,i} = D \cdot \varepsilon_i^{brugg}, \quad i = p, s, n$$

$$\sigma_{eff,i} = \sigma_i (1 - \varepsilon_i - \varepsilon_{f,i}), \quad i = p, n \quad a_i = \frac{3}{R_i} (1 - \varepsilon_i - \varepsilon_{f,i}), \quad i = p, s, n;$$

$$\theta_p = \frac{c^s|_{r=R_p}}{c_{\max,p}^s}; \quad \theta_n = \frac{c^s|_{r=R_n}}{c_{\max,n}^s}$$

$$\frac{\partial \delta}{\partial t} = \frac{j_{SEI} M_{SEI}}{\rho_{SEI}}$$

$$j_{SEI} = -\frac{\kappa_{SEI}}{F} \exp\left(-\alpha \frac{F}{RT} \left(\Phi_1 - \Phi_2 - U_{SEI} - \frac{\delta \cdot F \cdot (j_n + j_{SEI})}{\kappa_{SEI}} \right)\right)$$

ergy converted by the DC/AC inverter will be provided directly to users on the microgrid for any demand below the level of the solar power, and batteries will be charged with any power available above the level of demand. In contrast, when the converted solar power decreases below the desired level of demand, batteries will be discharged to provide the stored energy to the users. The bidirectional DC/DC converter is connected to batteries in the same manner as the PV systems' configuration. Also, the role of power electronics connected to

Table V. Governing equations for Li-ion P2D model.

Governing equation	Boundary conditions
<p>Positive</p> $\varepsilon_p \frac{\partial c}{\partial t} = \frac{\partial}{\partial x} [D_{eff,p} \frac{\partial c}{\partial x}] + a_p (1 - t_+) j_p$ $-\sigma_{eff,p} \left(\frac{\partial \Phi_1}{\partial x} \right) - \kappa_{eff,p} \left(\frac{\partial \Phi_2}{\partial x} \right) + \frac{2\kappa_{eff,p} RT}{F} (1 - t_+) \left(\frac{\partial \ln c}{\partial x} \right) = I$ $\frac{\partial}{\partial x} [\sigma_{eff,p} \frac{\partial \Phi_1}{\partial x}] = a_p F j_p$ $\frac{\partial}{\partial t} c_p^{s,ave} = -3 \frac{j_p}{R_p}, \quad \frac{D_{s,p}}{R_p} (c_p^{s,surf} - c_p^{s,ave}) = -\frac{j_p}{5}$	$\frac{\partial c}{\partial x} _{x=0} = 0$ $-D_{eff,p} \frac{\partial c}{\partial x} _{x=l_p^-} = -D_{eff,s} \frac{\partial c}{\partial x} _{x=l_p^+}$ $\frac{\partial \Phi_2}{\partial x} _{x=0} = 0$ $-\kappa_{eff,p} \frac{\partial \Phi_2}{\partial x} _{x=l_p^-} = -\kappa_{eff,s} \frac{\partial \Phi_2}{\partial x} _{x=l_p^+}$ $\frac{\partial \Phi_1}{\partial x} _{x=l_p^-} = 0$ $\frac{\partial \Phi_1}{\partial x} _{x=0} = -\frac{I}{\sigma_{eff,p}}$
<p>Separator</p> $\varepsilon_s \frac{\partial c}{\partial t} = \frac{\partial}{\partial x} [D_{eff,s} \frac{\partial c}{\partial x}]$ $-\kappa_{eff,s} \left(\frac{\partial \Phi_2}{\partial x} \right) + \frac{2\kappa_{eff,s} RT}{F} (1 - t_+) \left(\frac{\partial \ln c}{\partial x} \right) = I$	$c _{x=l_p^-} = c _{x=l_p^+}$ $c _{x=l_p+l_s^-} = c _{x=l_p+l_s^+}$ $\Phi_2 _{x=l_p^-} = \Phi_2 _{x=l_p^+}$ $\Phi_2 _{x=l_p+l_s^-} = \Phi_2 _{x=l_p+l_s^+}$
<p>Negative electrode</p> $\varepsilon_n \frac{\partial c}{\partial t} = \frac{\partial}{\partial x} [D_{eff,n} \frac{\partial c}{\partial x}] + a_n (1 - t_+) j_n$ $-\sigma_{eff,n} \left(\frac{\partial \Phi_1}{\partial x} \right) - \kappa_{eff,n} \left(\frac{\partial \Phi_2}{\partial x} \right) + \frac{2\kappa_{eff,n} RT}{F} (1 - t_+) \left(\frac{\partial \ln c}{\partial x} \right) = I$ $\frac{\partial}{\partial x} [\sigma_{eff,n} \frac{\partial \Phi_1}{\partial x}] = a_n F j_n$ $\frac{\partial}{\partial t} c_n^{s,ave} = -3 \frac{j_n}{R_n}, \quad \frac{D_{s,n}}{R_n} (c_n^{s,surf} - c_n^{s,ave}) = -\frac{j_n}{5}$	$\frac{\partial c}{\partial x} _{x=l_p+l_s+l_n} = 0$ $-D_{eff,s} \frac{\partial c}{\partial x} _{x=l_p+l_s^-} = -D_{eff,n} \frac{\partial c}{\partial x} _{x=l_p+l_s^+}$ $\Phi_2 _{x=l_p+l_s+l_n} = 0$ $-\kappa_{eff,s} \frac{\partial \Phi_2}{\partial x} _{x=l_p+l_s^-} = -\kappa_{eff,n} \frac{\partial \Phi_2}{\partial x} _{x=l_p+l_s^+}$ $\frac{\partial \Phi_1}{\partial x} _{x=l_p+l_s^-} = 0$ $\frac{\partial \Phi_1}{\partial x} _{x=l_p+l_s+l_n} = -\frac{I}{\sigma_{eff,n}}$

Table VII. List of variables for Li-ion P2D model.

Symbol	Variables	Units
c	Electrolyte concentration	mol/m ³
c_i^s	Solid phase concentration	mol/m ³
Φ_1	Solid phase potential	V
Φ_2	Liquid phase potential	V
$c_i^{s,surf}$	Solid phase concentration at surface	mol/m ³
$c_i^{s,ave}$	Average solid phase concentration	mol/m ³
I	Applied current density	A/m ²
U_i	Open circuit potential at positive ($i = p$) and negative ($i = n$)	V
j_i	Pore wall flux at positive ($i = p$) and negative ($i = n$)	mol/m ² /s
$\kappa_{eff,i}$	Liquid phase conductivity at positive ($i = p$), separator ($i = s$), and negative ($i = n$)	S/m
$D_{eff,i}$	Effective diffusion coefficient conductivity at positive ($i = p$), separator ($i = s$), and negative ($i = n$)	m ² /s
$\sigma_{eff,i}$	Effective solid phase conductivity at positive ($i = p$) and negative ($i = n$)	S/m
θ_i	State of charge at positive ($i = p$) and negative ($i = n$)	-
j_{SEI}	Flux associated with SEI layer growth	mol/m ² /s
c_{sol}	Concentration of solvent at anode surface	mol/m ³
c_{Li^+}	Concentration of electrolyte at anode surface	mol/m ³
δ	SEI layer thickness	m

batteries, the voltage value across the DC bus, and the bidirectional DC/AC inverter's conversion efficiency are assumed to be the same as the PV systems were described in the previous section. The DC/DC converter's equations are:²⁵

$$I_{dc,battery}(t) = (1 - D_{battery}(t)) \cdot I_{battery,out}(t) \quad [13]$$

$$V_{dc} = \frac{1}{1 - D_{battery}(t)} V_{battery,out}(t) \quad [14]$$

$$P_{in,battery}(t) = I_{dc,battery}(t) \cdot V_{dc} \quad [15]$$

$I_{dc,battery}(t)$ is the DC bus current, $V_{battery,out}(t)$ is the output voltage, $I_{battery,out}(t)$ is the output current, and $D_{battery}(t)$ is the duty ratio of the DC/DC converter, from batteries. For the bidirectional DC/AC inverter, the amount of DC/AC inverter's output power ($P_{out,battery}(t)$) supplied by batteries' power ($P_{in,battery}(t)$) can be calculated based on the relation between the input and output power in Equation 12 as shown below:

$$P_{out,battery}(t) = \eta \cdot P_{in,battery}(t) \quad [16]$$

$P_{out,battery}(t)$ is the output power from the DC/AC inverter, and $P_{in,battery}(t)$ is the input power from the DC/DC converter connected to batteries. Batteries are operated to make up the difference between the demand ($P_{demand}(t)$) and the PV arrays' power ($P_{out,PV}(t)$) converted by the DC/AC inverter.

$$P_{out,battery}(t) = P_{out,PV}(t) - P_{demand}(t) \quad [17]$$

By substituting Equations 12 and 16 into Equation 17, we get

$$P_{in,battery}(t) = P_{in,PV}(t) - \frac{P_{demand}(t)}{\eta} \quad [18]$$

Results.—The reformulated P2D model for single cathode/separator/anode cell sandwich was scaled up to a kilowatt-scale systems corresponding to the power level of PV systems and demands (assuming no loss in performance). A 1500 kWh sized battery with 10% initial state of charge (SOC) was used in the simulation to illustrate the efficiency of the P2D model along with the fast computation time in proposed microgrid controls. Cost and energy savings by implementing the proposed control strategy including the electrochemical engineering model and DAE-based MPPT algorithm is also presented. The demand starts at 12 PM and continues until 7 PM at a constant value (120 kW), as shown in Figure 9a. The total demand is 840 kWh. The power obtained from solar arrays, using the P&O and DAE-based MPPT algorithm, are 1307.96 kWh and 1308.89 kWh, respectively. The battery will be discharged when the demand is greater than the power supplied from solar arrays, and vice versa (see Figure 9b). In other words, when batteries' current is below zero, which means demand is greater than solar array's power, batteries are discharged. In Figures 9c and 9d, the reformulated P2D model predicts voltage and SOC accurately with reasonable CPU time. The

Table VIII. Parameters for Li-ion P2D model.

Symbol	Parameter	Positive Electrode	Separator	Negative Electrode	Units
σ_i	Solid phase conductivity	100		100	S/m
$\varepsilon_{f,i}$	Filler fraction	0.025		0.0326	-
ε_i	Porosity	0.385	0.724	0.485	-
$Brugg$	Bruggman Coefficient	4	4	4	-
D	Electrolyte diffusivity	7.5×10^{-10}	7.5×10^{-10}	7.5×10^{-10}	m ² /s
D_i^s	Solid Phase Diffusivity	1.0×10^{-14}		3.9×10^{-14}	m ² /s
k_i	Reaction Rate constant	2.334×10^{-11}		5.031×10^{-11}	m ^{2.5} /(mol ^{0.5} s)
$c_{i,max}^s$	Maximum solid phase concentration	51554		30555	mol/m ³
$c_{i,0}^s$	Initial solid phase concentration	25751		26128	mol/m ³
c_0	Initial electrolyte concentration	1000	1000	1000	mol/m ³
$R_{p,i}$	Particle Radius	2.0×10^{-6}		2.0×10^{-6}	m
a_i	Particle Surface Area to Volume	885000		723600	m ² /m ³
l_i	Region thickness	80×10^{-6}	25×10^{-6}	88×10^{-6}	m
t_+	Transference number		0.364		-
F	Faraday's Constant		96487		C/mol
R	Gas Constant		8.314		J/(mol · K)
T	Temperature		298.15		K
ρ	Density	2500	1100	2500	kg/m ³
k_{SEI}	Rate constant for SEI reaction			1.5×10^{-6}	A/m ²
α	Transfer coefficient	0.5		0.5	-
U_{SEI}	Open circuit potential for SEI layer			0.4	V
κ_{SEI}	Conductivity of SEI layer			1	S/m
ρ_{SEI}	Density of SEI layer			2.1×10^3	kg/m ³
M_{SEI}	Molecular weight of SEI layer			0.026	kg/mol

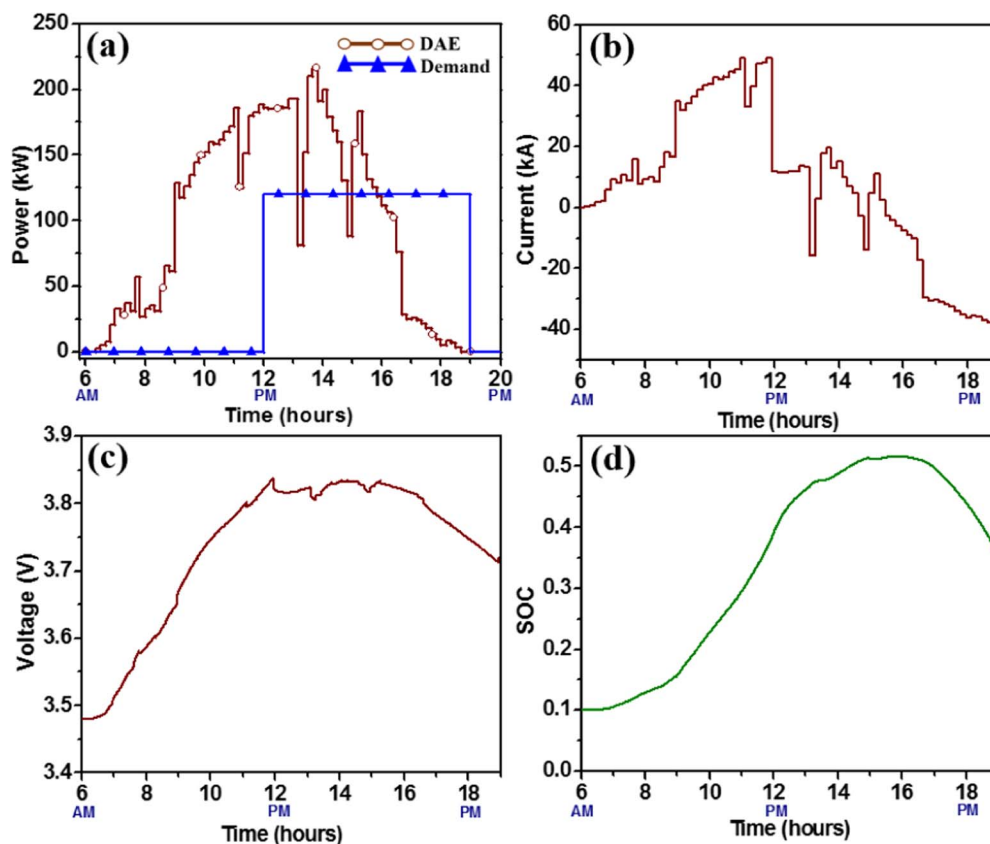


Figure 9. Performance of reformulated P2D battery model under dynamic irradiation condition. (a) Solar power outputs from DAE-based MPPT (wine color and empty circle) and demand (blue color and filled triangle). (b) Current outputs (c) Voltage outputs (d) SOC. The proposed approach enables aggressive control of batteries for microgrids as internal variables are predicted accurately in real-time.

proposed control scheme's running time is only 19.157 seconds for a single day simulation. As we mentioned before, lithium-ion batteries are the most expensive single component accounting for about 60% of overall CapEx among the whole microgrid components.⁵ Total costs of microgrids currently range between 583 and 1166 \$/kWh.⁵ Accordingly, total costs of the lithium-ion batteries in CapEx is between 350 and 700 \$/kWh. For example, if we can reduce the battery size by 50%, total cost of the battery system will decrease to

175–350 \$/kWh with significant reduction in total cost for large-scale microgrids.

Simple empirical/equivalent-circuit or black-box battery models will not be able to capture the essential dynamics of battery performance accurately and will provide poor estimates of cell size and costs. The proposed approach is fundamentally different from the existing microgrid control architecture. Instead of treating cells as a black box, critical internal states will be addressed with high accuracy and capable of being simulated in real-time. For example, SEI layer growth from the reformulated P2D battery model is presented in Figure 10. The SEI layer causes lithium ions' diffusion resistance and a voltage drop across the battery. Including the SEI layer growth as an internal variable can be used to control the capacity fade over cycles.³⁴ Even though capacity fade/degradation is accelerated by extreme charging patterns, increased temperature, and overcharging, the batteries degrade even under normal operation.

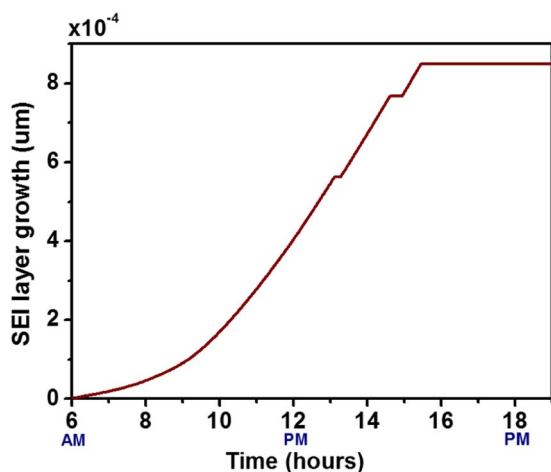


Figure 10. SEI layer growth predicted by the P2D battery model. The proposed approach enables real-time prediction of capacity degradation in a particular cycle. Fast simulation of degradation of batteries over multiple cycles will be useful for improving the life of the batteries for microgrid applications.

Practical Impact and Implementation into a Microcontroller

Current state of the art typically involves using empirical models for batteries in grid simulation. Recently, aggressive and efficient control strategies for grid and renewable grids are heavily supported by the U.S. Department of Energy.^{37,38} However, current perception amongst the grid community is that physics-based battery models are too complicated to be used in grid control. We hope that this paper shows that aggressive control strategies for renewable grids can benefit from real-time simulation of physics-based battery models. In this section, we illustrate that the DAE-based microgrid control can be implemented in a low cost microcontroller, while performing better than current microgrid algorithms. Lithium-ion battery packs in grid or otherwise are always connected to a Battery Management System (BMS). BMSs are devices that are responsible for safely operating the

battery.³⁹ With a microcontroller or a microprocessor onboard, a BMS can be made to operate the battery for satisfying desired control goals. To make the DAE-based microgrid control commercially viable, we must be able to simulate the model in a low cost microcontroller in real-time. As a proof-of-concept, we have used a BeagleBone Black (BBB) to represent such a microprocessor system with minimal computing specifications. BBB has 512 MB of onboard RAM with Cortex ARM processor running Linux⁴⁰ and is the size of a credit card. An open source free solver IDA, which is part of SUNDIALS,⁴¹ simulates the PV array with the DAE-based MPPT controller and power electronics (see Modeling of PV arrays with MPPT controller & power electronics components section) in 1.1 seconds and the implementation of the reformulated P2D battery model with other microgrid components (see Modeling of PV arrays with MPPT controller, battery & power electronics components section) in 2.8 seconds.

Conclusions

Batteries in the microgrid system need to be understood well for accurate characterization, and an intelligent management system to monitor and maintain economic, safe and optimal operations. Conventional battery controls in the microgrid only allow for meeting the power demand but lack predictability and accuracy. This work provides new insights for research on microgrid control strategy for the following reason: simultaneous modeling, simulation, and control by incorporating physics-based electrochemical engineering battery models along with PV arrays, DAE-based MPPT algorithm, and power electronics. Our findings show that the proposed microgrids control, including the DAE-based MPPT algorithm with the P2D battery model, is capable of saving a significant amount of energy and cost. Proposed controls approach would help optimize the performance of batteries in microgrids. Also, proposed controls simulate the performance of individual components in the microgrid simultaneously and meet the grid constraints. Our current and future work involves performing optimal and model predictive control strategies to improve the performance of battery stacks for grid applications for improved life, deeper depth of discharge, reduced levelized cost, and to enable and benefit from two bidirectional flow of information, energy and control actions from both batteries and the rest of the grid. Advanced controls based on proposed modeling and control techniques would reduce the induced degradation of batteries and improve the performance of the overall microgrid system.

Acknowledgments

This work was supported by the Clean Energy Institute located in University of Washington, Seattle and Washington Research Foundation. The battery modeling work has been supported by the Assistant Secretary for Energy Efficiency and Renewable Energy, Office of Vehicle Technologies of the U. S. Department of Energy through the Advanced Battery Material Research (BMR) Program (Battery500 Consortium). The authors acknowledge the reviewers for their critical feedback which helped in improving the quality of the manuscript. VS wants to thank Matt Lawder, a past PhD student who initiated the task of integrating battery models with solar models.

References

1. B. Dunn, H. Kamath, and J.-M. Tarascon, *Science*, **334**(6058), 928 (2011).
2. M. Beaudin, H. Zareipour, A. Schellenbergglabe, and W. Rosehart, *Energy for Sustainable Development*, **14**(4), 302 (2010).
3. K. Divya and J. Ostergaard, *Electric Power Systems Research*, **79**(4), 511 (2009).

4. S. Lacey, Greentech Media, USA, 2016. Available: <https://www.greentechmedia.com/articles/read/stem-cto-weve-seen-battery-prices-fall-70-in-the-last-18-months>.
5. N. Ivanova, *Energy storage update*, London, UK, 2015. Available: <http://analysis.energystorageupdate.com/lithium-ion-costs-fall-50-within-five-years>.
6. D. A. Beck, J. M. Carothers, V. R. Subramanian, and J. Pfäendner, *AIChE Journal*, **62**(5), 1402 (2016).
7. X. Li, *IET Renewable Power Generation*, **6**(5), 340 (2012).
8. X. Li, D. Hui, and X. Lai, *IEEE Transactions on Sustainable Energy*, **4**(2), 464 (2013).
9. X. Li, Y. Li, X. Han, and D. Hui, *Energy Procedia*, **12** 994 (2011).
10. P. Naderi, *Journal of Solar Energy Engineering*, **135**(2), 024506 (2013).
11. G. G. Botte, V. R. Subramanian, and R. E. White, *Electrochimica Acta*, **45**(15), 2595 (2000).
12. V. Tamrakar, S. C. Gupta, and Y. Sawle, *Electrical and Electronics Engineering: An International Journal (EELIJ)*, **4**(3), (2015).
13. M. G. Villalva, J. R. Gazoli, and E. Ruppert Filho, *IEEE Transactions on Power Electronics*, **24**(5), 1198 (2009).
14. N. Femia, G. Petrone, G. Spagnuolo, and M. Vitelli, *IEEE transactions on Power Electronics*, **20**(4), 963 (2005).
15. N. Zakzouk, A. Abdelsalam, A. Helal, and B. Williams, in "*Industrial Electronics Society, IECON 2013-39th Annual Conference of the IEEE*, Vienna, Austria", p. 1741. IEEE, 2013.
16. N. Femia, D. Granozio, G. Petrone, G. Spagnuolo, and M. Vitelli, *IEEE Transactions on Aerospace and Electronic Systems*, **43**(3), 934 (2007).
17. J. J. Nedumgatt, K. Jayakrishnan, S. Umashankar, D. Vijayakumar, and D. Kothari, in "*2011 Annual IEEE India Conference*", p. 1. IEEE, 2011.
18. L. Piegari and R. Rizzo, *IET Renewable Power Generation*, **4**(4), 317 (2010).
19. D. Sera, L. Mathe, T. Kerekes, S. V. Spataru, and R. Teodorescu, *IEEE Journal of Photovoltaics*, **3**(3), 1070 (2013).
20. C. W. Tan, T. C. Green, and C. A. Hernandez-Aramburo, in "*Power and Energy Conference, 2008. PESC 2008. IEEE 2nd International, Johor Bahru, Malaysia*", p. 237. IEEE, 2008.
21. V. Salas, E. Olias, A. Barrado, and A. Lazaro, *Solar energy materials and solar cells*, **90**(11), 1555 (2006).
22. R. N. Methekar, V. Ramadesigan, J. C. Pirkle, and V. R. Subramanian, *Computers & Chemical Engineering*, **35**(11), 2227 (2011).
23. *Measurement and Instrumentation Data Center, National Renewable Energy Laboratory*, 2014. Available: <http://www.nrel.gov/midc/>.
24. H. Tao, A. Kotsopoulos, J. L. Duarte, and M. A. Hendrix, *IEE Proceedings-Electric Power Applications*, **153**(3), 451 (2006).
25. M. R. Islam, Y. Guo, and J. Zhu, in *Power Converters for Medium Voltage Networks*, p. 17, Springer, (2014).
26. P. W. Northrop, V. Ramadesigan, S. De, and V. R. Subramanian, *Journal of The Electrochemical Society*, **158**(12), A1461 (2011).
27. M. T. Lawder, V. Ramadesigan, B. Suthar, and V. R. Subramanian, *Computers & Chemical Engineering*, **82** 283 (2015).
28. C. S. Chim, P. Neelakantan, H. P. Yoong, and K. T. K. Teo, in "*2011 UkSim 13th International Conference on Computer Modelling and Simulation*, Cambridge, UK", p. 376. IEEE, 2011.
29. R. Rawat and S. Chandel, *Int. J. Sustain. Dev. Green Econ. (IJSDEG)*, **2**, 90 (2013).
30. B. Subudhi and R. Pradhan, *IEEE Transactions on Sustainable Energy*, **4**(1), 89 (2013).
31. L. F. Shampine, M. W. Reichelt, and J. A. Kierzenka, *SIAM review*, **41**(3), 538 (1999).
32. M. Doyle, T. F. Fuller, and J. Newman, *Journal of the Electrochemical Society*, **140**(6), 1526 (1993).
33. S. Santhanagopalan, Q. Guo, P. Ramadass, and R. E. White, *Journal of Power Sources*, **156**(2), 620 (2006).
34. M. T. Lawder, B. Suthar, P. W. Northrop, S. De, C. M. Hoff, O. Leitermann, M. L. Crow, S. Santhanagopalan, and V. R. Subramanian, *Proceedings of the IEEE*, **102**(6), 1014 (2014).
35. M. B. Pinson and M. Z. Bazant, *Journal of the Electrochemical Society*, **160**(2), A243 (2013).
36. P. Ramadass, B. Haran, P. M. Gomadam, R. White, and B. N. Popov, *Journal of the Electrochemical Society*, **151**(2), A196 (2004).
37. Network Optimized Distributed Energy Systems (NODES), U.S. Department of Energy (DOE). Available: <https://arpa-e.energy.gov/?q=arpa-e-programs/nodes>.
38. Enabling Extreme Real-Time Grid Intergration of Solar Energy (ENERGISE), U.S. Department of Energy (DOE). Available: <https://energy.gov/eere/sunshot/enabling-extreme-real-time-grid-integration-solar-energy-energise>.
39. M. Brandl, H. Gall, M. Wenger, V. Lorentz, M. Giegerich, F. Baronti, G. Fantechi, L. Fanucci, R. Roncella, and R. Saletti, in "*Design, Automation & Test in Europe Conference & Exhibition (DATE)*, Dresden, Germany, 2012", p. 971. IEEE, 2012.
40. G. Coley, *Beaglebone black system reference manual*, Texas Instruments, Dallas (2013). Available: <http://elinux.org/Beagleboard:BeagleBoneBlack>.
41. A. C. Hindmarsh, R. Serban, and A. Collier, *User Documentation for ida v2. 6.0*, Center for Applied Scientific Computing Lawrence Livermore National Laboratory (2006).